Analytical study on growth-induced axisymmetric deformations and shape-control of circular hyperelastic plates

Zhanfeng Li[a], Qiongyu Wang[a,c], Ping Du[a], Chennakesava Kadapa[d],
Mokarram Hossain[e], Jiong Wang[a,b,*]

[a]*School of Civil Engineering and Transportation, South China University of
Technology, Guangzhou, 510640, Guangdong, China*
[b]*State Key Laboratory of Subtropical Building Science, South China University of
Technology, Guangzhou, 510640, Guangdong, China*
[c]*China Communications Construction Company, Fourth Harbor Engineering Institute
Co., Ltd, Guangzhou, 510230, Guangdong, China*
[d]*School of Engineering, University of Bolton, Bolton, BL3 5AB, United Kingdom*
[e]*Zienkiewicz Centre for Computational Engineering (ZCCE), Swansea
University, Swansea, SA1 8EN, United Kingdom*

Abstract

Growth of soft material plates is commonly observed in nature. However, the relations between growth fields and shape changes of the plates remain poorly understood. The current work aims to derive some analytical results for the growth-induced axisymmetric deformations of circular hyperelastic plates. The problem of shape-control of circular plates through differential growth will also be studied. First, starting from the 3D governing system, we formulate the 2D vector plate equation system through a series expansion and truncation approach. Under the assumption of axisymmetric deformation, the plate equations can be solved analytically. Some analytical (asymptotic) solutions are derived for both the out-of-plane bending deformation and the in-plane flat deformation of the plate, which can fit the numerical results quite well. By comparing the energy densities, the preferred deformation style of the plate corresponding to any given growth functions can be determined, based on which the combined bending-flat deformation of the plate

---

[*]Corresponding author
Email address: `ctjwang@scut.edu.cn` (Jiong Wang)

is also studied. Furthermore, by solving an inverse problem, we derived the explicit formula for shape-control of thin circular hyperelastic plates. With this formula, most of the 3D axisymmetric configurations can be generated by selecting proper growth functions in the plates. The results obtained in the current work can not only reveal the mechanisms of growth-induced deformations of soft material samples, but also have wide potential applications in the manufacture of intelligent soft devices.

1. Introduction

Growth (or atrophy) of soft biological tissues is commonly observed in nature. Due to the inhomogeneous or incompatibility of the growth fields, i.e., the so called differential growth, the tissues usually exhibit diverse geometrical shape changes and surface pattern evolution during the growing processes (Li et al., 2012; Menzel and Kuhl, 2012; Huang et al., 2018; Ambrosi et al., 2019). The mechanisms of differential growth and their effects on the shape formations of soft biological tissues have attracted extensive research interests. Besides the factors of genetics (Coen et al., 2004; Whitewoods et al., 2020), biochemistry (Green, 1996) and environmental stimuli (van Doorn and Kamdee, 2014; Moulton et al., 2020; Moulia et al., 2021), these problems have also been extensively studied from the aspect of mechanics (Liang and Mahadevan, 2011; Budday et al., 2014; Goriely, 2017; Ben Amar et al., 2019; Liu et al., 2020; Xu et al., 2020; Chen et al., 2021). On the other hand, the properties of swelling (or shrinking) of soft materials (e.g., hydrogels, polymers) under suitable external stimuli have also attracted much research interests in the engineering fields (Ionov, 2013; Kempaiah and Nie, 2014; Hossain et al., 2010). Through elaborate design of the compositions or architectures in the soft material samples, the different sample regions can possess different swelling ratios, which result in various shape changes of the samples (Liu et al., 2016; Siéfert et al., 2019). This procedure is known as shape-programming/shape-control, and it has been utilized for the manufacture of intelligent soft devices, e.g., soft robots (Lee et al., 2010; Shepherd et al., 2011), 4D printing biomimetic flowers (Gladman et al., 2016), self-folding microgrippers (Abdullah et al., 2018).

2

To reveal the mechanisms of growth-induced deformations of soft biological tissues, or to fulfill the requirements of manufacture of intelligent soft devices, one central but non-trivial task is to find out the relations between the growth (swelling) fields and the shape changes of soft material samples, corresponding to different sample configurations, growing styles and environmental conditions. To accomplish this task, a reliable and accurate mathematical model is necessary.

In many of the existing models, large deformable soft materials are treated as hyperelastic materials (Ben Amar and Goriely, 2005; Goriely, 2017; Hossain and Steinmann, 2013; Mihai et al., 2017). To describe the growing processes, the total deformation gradient tensor is usually decomposed into the multiplication of an elastic deformation tensor and a growth tensor (Kondaurov and Nikitin, 1987; Rodriguez et al., 1994). Another mathematically rigorous modeling approach was proposed based on the geometric theory (Efrati et al., 2009b; Yavari, 2010), where the growth effect is interpreted as the metric evolution in the material manifolds. As the elastic deformations of soft materials are generally isochoric, the constraint equation of elastic incompressibility should be adopted. To represent the effect of differential growth, the growth fields in the soft material samples are set to be incompatible, which will induce residual stresses and result in large deformations of the samples (Skalak et al., 1996; Jones and Chapman, 2012; Lee et al., 2021). By choosing suitable constitutive relations and through some conventional derivations, the mechanical field equation and the associated boundary conditions are obtained, which together with the elastic incompressibility equation formulate the governing system for modeling the mechanical behaviors of soft material samples. The governing equation system can be solved through various analytical or numerical approaches (Chen and Dai, 2020; Kadapa et al., 2021; Wang et al., 2021), then the growing processes of the samples will be described. Furthermore, to capture the mechanical instability phenomena in biological tissues, the bifurcation properties of the governing system need to be investigated (Li et al., 2012; Goriely, 2017).

Usually, the soft material samples that undergo significant shape changes during growth (or swelling) have the thin plate or shell forms (e.g., leaves, petals, peels, and animal skins). To study the mechanical behaviors of these samples, one needs to adopt a suitable plate or shell theory. In the literature, the well known Föppl-von Kármán (FvK) plate theory has been successfully applied to study the growth-induced deformations or other mechanical behaviors of soft material samples (Dervaux et al., 2009; Jones and Mahadevan,

2015; Huang et al., 2016; Mihai and Goriely, 2020). Although the FvK plate theory has been widely accepted and utilized, it involves a priori assumption on the displacements and has limitations for the problems of finite-strain elasticity. Some other plate or shell models with growth effect were established based on the non-Euclidean geometric theory (Efrati et al., 2009b,a; Sadik et al., 2016), which incorporate the geometric quantities, such as the first and second fundamental forms, to describe the growth-induced shape changes of plate or shell samples. In Dai and Song (2014) and Wang et al. (2016), a consistent finite-strain plate theory was proposed for both compressible and incompressible elastic materials, which was derived from the 3D governing system through a series expansion and truncation approach. This plate theory was further extended in Wang et al. (2018) to incorporate the growth effects. Recently, this plate theory has been applied to study the plane-strain problems of growth-induced deformations in single- and multi-layered hyperelastic plates (Wang et al., 2019; Du et al., 2020). To model the growth-induced deformations of soft material plates or shells, the established plate or shell equation systems are usually some complicated nonlinear PDE system, which are difficult to be solved analytically. Currently, the analytical results reported in the literature are still rare (Dias et al., 2011; Goriely, 2017; Wang et al., 2019; Chen et al., 2021). Especially, the explicit relations between the growth fields and shape changes of soft material samples remain poorly understood.

In the current work, we aim to derive some analytical results for growth-induced axisymmetric deformations of circular hyperelastic plates. The problem of shape-control of circular plates through differential growth will also be studied. The basis of the current work is a 2D plate equation system, which is derived from the 3D governing system through the approach introduced in Wang et al. (2018). Under the assumption of axisymmetric deformations, the plate equations are solved analytically. With the obtained solutions, the 3D configurations of the plate samples can also be recovered. Through the comparisons with the numerical results, it will be seen that the analytical solutions can provide accurate predictions on the growth-induced deformations of the plate. Especially, for any given growth functions, the features of deformation of the plate, i.e., out-of-plane bending deformation or in-plane flat deformation (extension/contraction in radial direction), can be determined in advance. Furthermore, by solving an inverse problem, we derived the explicit formula for shape-control of thin circular hyperelastic plates, based on which most 3D axisymmetric configurations can be generated by properly

4

setting the growth functions in the plate samples.

This paper is organized as follows. In Section 2, the plate equations for modeling the growth-induced deformations of a circular hyperelastic plate is derived. In section 3, the axisymmetric deformations of the plate is studied based on the plate equations, from which some analytical results are obtained. In section 4, the problem of shape-control of circular hyperelastic plates is solved. Finally, some conclusions are drawn.

2. Plate equation system

We consider a thin circular hyperelastic plate with a constant thickness. Within a 3D cylindrical coordinate system, suppose the reference configuration of the plate occupies the region $\kappa_r = \Omega_r \times [0, 2h] = [R_0, R_1] \times [0, 2\pi] \times [0, 2h]$ (cf. Fig.1A), where R_0 and R_1 are the inner and outer radii of the in-plane area Ω_r, respectively. The thickness $2h$ is relatively small compared to the dimension of Ω_r. At a material point with coordinates (R, Θ, Z) in κ_r, the unit vectors directing along the cylindrical coordinate axes are denoted as $\{\mathbf{e}_R, \mathbf{e}_\Theta, \mathbf{e}_Z\}$. Then, the referential position vector of the material point can be denoted as $\mathbf{X} = R\mathbf{e}_R + Z\mathbf{e}_Z$.
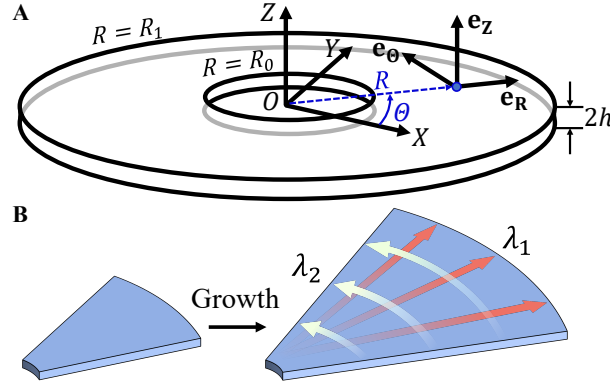

Figure 1: Illustrations of the reference configuration of the thin circular hyperelastic plate and the growth field in the plate: (A) The reference configuration κ_r of the plate; (B) Distributions of the growth functions $\lambda_1(R)$ along the radial direction and $\lambda_2(R)$ along the circumferential direction.

During the growing process, there is no external traction or boundary constraint applied on the plate. Growth of the plate sample occurs along the radial and the circumferential directions, which is represented by the

growth functions $\lambda_1(R)$ and $\lambda_2(R)$, respectively (cf. Fig.1B). Notice that these growth functions do not depend on the coordinates Θ and Z. Due to the incompatibility of the growth field, some residual stresses will be activated, which can further induce shape change or pattern evolution of the plate. After the deformation, the plate attains the current configuration κ_t. Suppose the material point initially locating at (R, Θ, Z) in κ_r has the new position (r, θ, z) in κ_t. In this work, we only focus on the growth-induced axisymmetric deformation of the plate, which implies that $\theta = \Theta$. In terms of the unit vectors $\{\mathbf{e}_r, \mathbf{e}_\theta, \mathbf{e}_z\}$ along the cylindrical coordinate axes, the current position vector of the material point can be denoted as $\mathbf{x} = r\mathbf{e}_r + z\mathbf{e}_z$.

With the given position vectors $\mathbf{X}$ and $\mathbf{x}$, the deformation gradient tensor $\mathbb{F}$ can be calculated through $\mathbb{F} = \dfrac{\partial \mathbf{x}}{\partial \mathbf{X}} = \nabla \mathbf{x} + \dfrac{\partial \mathbf{x}}{\partial Z}\mathbf{e}_Z$, where '$\nabla$' is the in-plane 2D gradient operator. Following the approach of Rodriguez et al. (1994), $\mathbb{F}$ is decomposed as $\mathbb{F} = \mathbb{A}\mathbb{G}$, where $\mathbb{A}$ is the elastic deformation tensor and $\mathbb{G}$ is the growth tensor. Corresponding to the biaxial growth of the plate in the radial and circumferential directions, the growth tensor is given by $\mathbb{G} = \text{diag}\left(\lambda_1(R), \lambda_2(R), 1\right)$. It should be noted that the growth tensor $\mathbb{G}$ is prescribed locally at each material point, which is irrespective of the growth conditions of neighboring points and the global geometry of the sample. In the case that $\mathbb{G}$ does not satisfy the compatibility condition $\nabla \times \mathbb{G} = 0$ (cf. Yavari, 2013), there is no real intermediate configuration κ_m exists such that the deformation gradient from κ_r to κ_m is given by $\mathbb{G}$. Thus, to ensure the integrity of the whole configuration of the plate, the elastic deformation will take place simultaneously and some residual stresses will be activated in the plate.

As the elastic deformations of soft materials (e.g., soft biological tissues, polymeric gels) are generally isochoric, we adopt the following constraint equation

$$R(\mathbb{F}, \mathbb{G}) = R_0(\mathbb{A}) = \text{Det}(\mathbb{A}) - 1 = 0. \tag{1}$$

To obtain some concrete results, we further assume that the plate is made of an incompressible neo-Hookean material with the elastic strain-energy function $\phi(\mathbb{F}, \mathbb{G}) = J_G\phi_0(\mathbb{A}) = J_G C_0\left(\text{tr}(\mathbb{A}\mathbb{A}^T) - 3\right)$, where $J_G = \text{Det}(\mathbb{G})$ and C_0 is a material constant. The nominal stress tensor $\mathbb{S}$ of the material has the constitutive relation

$$\mathbb{S} = J_G\mathbb{G}^{-1}\left(2C_0\mathbb{A}^T - p(\mathbf{X})\mathbb{A}^{-1}\right), \tag{2}$$

6

where $p(\mathbf{X})$ is the Lagrange multiplier enforcing the incompressibility constraint (1).

The mechanical behavior of the circular hyperelastic plate should satisfy the following mechanical equilibrium equation

$$\mathrm{Div}\,\mathbb{S} = \mathbf{0}, \quad \mathrm{in} \;\; \Omega_r \times [0, 2h], \tag{3}$$

and the traction-free boundary conditions

$$\mathbb{S}^T \mathbf{e_R}\big|_{R=R_0,R_1} = \mathbf{0}, \quad \mathbb{S}^T \mathbf{e_Z}\big|_{Z=0,2h} = \mathbf{0}. \tag{4}$$

Eqs. (1)-(4) constitute the 3D governing system of the model.

Starting from the 3D governing system, a finite-strain plate equation system can be derived. The detailed derivation procedure of the plate equation system in a more general case can be found in Wang et al. (2018). For being self-contained of the current paper, a simple introduction on the derivation approach is given below.

First, by assuming sufficient smoothness, we develop the following series expansions of $\{r, z, p\}$ along the thickness direction (i.e., the Z-axis) of the plate:

$$r = \sum_{n=0}^{2} \frac{r^{(n)}}{n!} Z^n + O(Z^3), \;\; z = \sum_{n=0}^{2} \frac{z^{(n)}}{n!} Z^n + O(Z^3), \;\; p = \sum_{n=0}^{2} \frac{p^{(n)}}{n!} Z^n + O(Z^3), \tag{5}$$

where $(\cdot)^{(n)} = \partial^n(\cdot)/\left.\partial Z^n\right|_{Z=0}$. Actually, (5) assumes the the variations of $\{r, z, p\}$ along Z follow series form, which is a key step to transform the 3-D equilibrium equation into 2-D. Accordingly, the deformation gradient tensor $\mathbb{F}$, the elastic deformation tensor $\mathbb{A}$ and the nominal stress tensor $\mathbb{S}$ can also be expanded as

$$\begin{aligned}
\mathbb{F} &= \mathbb{F}^{(0)} + Z\mathbb{F}^{(1)} + O(Z^2), \\
\mathbb{A} &= \mathbb{A}^{(0)} + Z\mathbb{A}^{(1)} + O(Z^2), \\
\mathbb{S} &= \mathbb{S}^{(0)} + Z\mathbb{S}^{(1)} + O(Z^2).
\end{aligned} \tag{6}$$

Then equilibrium equation (3) can be expressed as $\nabla \cdot \mathbb{S}^{(n)} + (\mathbb{S}^{(n+1)})^T \mathbf{e}_Z = 0$. Substituting $\mathbb{A} = \mathbb{F}\mathbb{G}^{-1}$ into the constitutive relation (2), one can obtain the expressions of $\mathbb{S}^{(0)}$ and $\mathbb{S}^{(1)}$ (e.g., the components of $\mathbb{S}^{(0)}$ are presented in Appendix A).

Second, we substitute (5) into the constraint equation (1), the mechanical equilibrium equation (3) and the bottom boundary condition (4)$_2$ at $Z = 0$.

By considering the coefficients of Z^n, we establish a linear algebraic system for $r^{(1)}$-$r^{(2)}$, $z^{(1)}$-$z^{(2)}$ and $p^{(0)}$-$p^{(1)}$, from which the expressions of these unknowns in terms of $r^{(0)}$, θ and $z^{(0)}$ can be obtained. For example, $r^{(1)}$, $z^{(1)}$ and $p^{(0)}$ are given by

$$r^{(1)} = -\frac{z_{,R}^{(0)}}{\mathcal{B}_1}, \quad z^{(1)} = \frac{r_{,R}^{(0)}}{\mathcal{B}_1}, \quad p^{(0)} = \frac{2C_0 R\lambda_1\lambda_2}{\mathcal{B}_1 r^{(0)}}, \tag{7}$$

where

$$\mathcal{B}_1 = \frac{r^{(0)}}{R\lambda_1\lambda_2}\left(r_{,R}^{(0)\,2} + z_{,R}^{(0)\,2}\right)$$

Here, the subscript 'R' denote the derivative with respect to the variable R.

Third, by subtracting the boundary conditions given in $(4)_2$ and through some further manipulations, we can obtain the following 2D plate equation system

$$\nabla \cdot \overline{\mathbb{S}} = 0, \quad \text{in} \ \ \Omega_r, \tag{8}$$

where

$$\overline{\mathbb{S}} = \frac{1}{2h}\int_0^{2h} \mathbb{S}dZ = \mathbb{S}^{(0)} + h\mathbb{S}^{(1)} + O\left(h^2\right). \tag{9}$$

Eq. (9) provides three equations for the three unknowns $r^{(0)}$, θ and $z^{(0)}$. To complete the plate equation system, we propose the following traction-free boundary conditions

$$\left.\overline{\mathbb{S}}^T \mathbf{e_R}\right|_{R=R_0,R_1} = \mathbf{0}. \tag{10}$$

Sometimes, the bending moment applied on the edge of the plate also needs to be considered, which yields that

$$\mathbf{M}_h|_{R=R_0,R_1} = \mathbf{0}, \tag{11}$$

where

$$\mathbf{M}_h = \frac{1}{2h}\int_0^{2h}\left(\mathbb{S}^T\mathbf{e_R}\right)\wedge\left[\mathbf{x}(R,\Theta,Z) - \mathbf{x}(R,\Theta,h)\right]dZ$$

is the average value of the bending moment about the middle plane $Z = h$ of the plate, and $'\wedge'$ is the vector cross product operator.

3. Axisymmetric deformation and analytical results

In this section, we begin to study the axisymmetric deformation of the plate, which implies that $r^{(0)}$ and $z^{(0)}$ only depend on the coordinates $\{R, Z\}$. Accordingly, stress components are independent from Θ and there are only five possible nonzero components of stress($S_{Rr}, S_{Rz}, S_{\Theta\theta}, S_{Zr}$ and S_{Zz}), since radial stress in the plate will induce stress in circumferential direction. In this case, one of the plate equation in (8) is automatically satisfied and the other two plate equations can be written as

$$\frac{d}{dR}\left[R\left(S_{Rr}^{(0)} + hS_{Rr}^{(1)}\right)\right] - \left(S_{\Theta\theta}^{(0)} + hS_{\Theta\theta}^{(1)}\right) = 0,$$
$$\frac{d}{dR}\left[R\left(S_{Rz}^{(0)} + hS_{Rz}^{(1)}\right)\right] = 0,$$

(12)

where the terms of $O(h^2)$ have been dropped. The stress components $S_{Rr}^{(0)}$, $S_{\Theta\theta}^{(0)}$ and $S_{Rz}^{(0)}$ can be expressed in terms of $r^{(0)}$ and $z^{(0)}$ as

$$S_{Rr}^{(0)} = \frac{2C_0\lambda_2 r_{,R}^{(0)}}{\lambda_1}\left[1 - \frac{R^2\lambda_1{}^4\lambda_2{}^2}{r^{(0)2}\left(r_{,R}^{(0)2} + z_{,R}^{(0)2}\right)^2}\right],$$

$$S_{\Theta\theta}^{(0)} = \frac{2C_0 r^{(0)}\lambda_1}{R\lambda_2} - \frac{2C_0 R^3\lambda_1{}^3\lambda_2{}^3}{r^{(0)3}\left(r_{,R}^{(0)2} + z_{,R}^{(0)2}\right)},$$

(13)

$$S_{Rz}^{(0)} = \frac{2C_0\lambda_2 z_{,R}^{(0)}}{\lambda_1}\left[1 - \frac{R^2\lambda_1{}^4\lambda_2{}^2}{r^{(0)2}\left(r_{,R}^{(0)2} + z_{,R}^{(0)2}\right)^2}\right].$$

The expressions of stress components $S_{Rr}^{(1)}$, $S_{\Theta\theta}^{(1)}$ and $S_{Rz}^{(1)}$ have some complex forms, which are put in Appendix A for brevity.

Eq. (12) is still a coupled nonlinear PDE system, which is generally difficult to be solved analytically. However, (12)$_2$ can be integrated with respect to R and the integration constant should be zero according to the boundary condition (10). By virtue of this fact, we try to derive the asymptotic solutions to the plate equation system, based on which the growth-induced deformation of the plate can be described. For that purpose, we further conduct the following asymptotic expansions

$$r^{(0)} = r_0^{(0)} + hr_0^{(1)} + O(h^2),$$
$$z^{(0)} = z_0^{(0)} + hz_0^{(1)} + O(h^2).$$

(14)

9

Compared with (5), the meaning of (14) is to describe the effect of plate thickness h in an asymptotic manner.

3.1. Out-of-plane bending deformation

First, we consider the case $z_{0,R}^{(0)} \neq 0$, which corresponds to the out-of-plane bending deformation of the plate. By substituting (14) into the plate equation system (12) and solving the equations with the leading-order terms (i.e., the terms of $O(h^0)$), we can derive the following analytical solution

$$r_0^{(0)} = F(R), \quad z_0^{(0)} = c_z + \int_{R_0}^{R} \pm\sqrt{\lambda_1^2 - F_{,R}^2}dR, \tag{15}$$

where $F(R) = R\lambda_2(R)$ and c_z is an integration constant representing the rigid body motion of the plate. With this solution, it can be verified that all the components of $\mathbb{S}^{(0)}$ are equal to zero, thus the traction-free boundary condition (10) and moment boundary condition (11) are also satisfied automatically. Based on the solution (15), a necessary condition for the appearance of the bending deformation of the plate can be proposed (under the assumption of axisymmetric deformation). That is, if the quantity $\Delta = \lambda_1^2 - F_{,R}^2 > 0$, the plate may undergo the out-of-plane bending deformation. While, if $\Delta \leq 0$, the plate can only undergo the in-plane flat deformation.

For a relatively thin plate, the solution (15) can already provide good predictions on the growth-induced deformations of the plate. To obtain some more accurate analytical results, we further solve the plate equation system (12) including the terms of $O(h)$. By substituting (14) into (12) and through a regular perturbation method, the following asymptotic solution is obtained

$$r^{(0)} = F(R) + h\frac{\sqrt{\lambda_1^2 - F_{,R}^2}}{\lambda_1},$$
$$z^{(0)} = c_z + \int_{R_0}^{R} \pm\sqrt{\lambda_1^2 - F_{,R}^2}dR - h\frac{F_{,R}}{\lambda_1}. \tag{16}$$

With this solution, it can be verified that the nonzero stress components in the plate have order $O(h)$, which are distributed symmetrically with respect to the middle plane $Z = h$. Therefore, the boundary condition (10) is still satisfied. But the moment boundary condition (11) is not satisfied since there is small moment in order $O(h^2)$ on lateral faces of plate. By substituting (16)

10

into (7), we obtain the expressions of $r^{(1)}$ and $z^{(1)}$, then the 3D configuration of the plate can also be recovered.

To demonstrate the accuracy of the asymptotic solution (16), we introduce some typical examples. In these examples, we consider three circular hyperelastic plates with inner radius $R_0 = 0.2$, outer radius $R_1 = 1.2$. The thicknesses of the plates are set to be $2h = 0.001$, 0.05 and 0.1. Three sets of growth functions $\{\lambda_1, \lambda_2\}$ are selected for demonstration, which are given in Eqs. (17)-(19). All of these growth functions satisfy the condition $\Delta > 0$ in the whole plate region $[R_0, R_1]$. The position fields $\{r^{(0)}, z^{(0)}\}$ in the plate can be calculated with the solution (16) (where we assume $z^{(0)}_{0,R} > 0$), which are also presented in (17)-(19).

- Case 1-1:

$$
\begin{cases}
\lambda_1 = \dfrac{3}{2}, & \lambda_2 = 1, \\
r^{(0)} = R + \dfrac{\sqrt{5}}{3}h, & z^{(0)} = \dfrac{5R - 1}{2\sqrt{5}}.
\end{cases}
\tag{17}
$$

- Case 1-2:

$$
\begin{cases}
\lambda_1 = 1 + \dfrac{R^2}{2}, & \lambda_2 = 1, \\
r^{(0)} = R + h\dfrac{R\sqrt{R^2 + 4}}{R^2 + 2}, \\
z^{(0)} = \dfrac{1}{6}\left(R^2 + 4\right)^{3/2} - \dfrac{101\sqrt{101}}{750} - h\left(\dfrac{2}{R^2 + 2} + \dfrac{50}{51}\right).
\end{cases}
\tag{18}
$$

- Case 1-3:

$$
\begin{cases}
\lambda_1 = \dfrac{33R^2}{10} - \dfrac{28R}{25} + \dfrac{433}{250}, \quad \lambda_2 = R^2 + \dfrac{3}{4}, \\[2mm]
r^{(0)} = R\left(R^2 + \dfrac{3}{4}\right) + \dfrac{h}{10R(165R - 56) + 866} \\[2mm]
\qquad \sqrt{[10R(15R - 56) + 491]\,[70R(45R - 8) + 1241]}, \\[2mm]
z^{(0)} = \displaystyle\int_{R_0}^{R} \dfrac{1}{500}\Big[(150R^2 - 560R + 491) \\[2mm]
\qquad \times (3150R^2 - 560R + 1241)\Big]^{\frac{1}{2}}\mathrm{d}R \\[2mm]
\qquad - h\left(\dfrac{375\,(4R^2 + 1)}{10R(165R - 56) + 866} - \dfrac{87}{164}\right).
\end{cases}
\tag{19}
$$

With the solutions given in (17)-(19), the growth-induced deformations of the hyperelastic plates can be predicted. For the purpose of comparison, we also conduct finite element simulations on the deformations of the plates corresponding to the three sets of growth functions. A modified compressible neo-Hookean material model is implemented in the UMAT subroutine of ABAQUS. During the numerical calculations, the UMAT subroutine is called at each Gauss (integration) point. In the subroutine, the total deformation gradient tensor $\mathbb{F}$ is input from the finite element program. The growth functions $\lambda_1(R)$ and $\lambda_2(R)$ are chosen as the state variables, whose values at the Gauss point are also input into the subroutine. Then, the elastic strain tensor is calculated from $\mathbb{A} = \mathbb{F}\mathbb{G}^{-1}$ ($\mathbb{G} = \mathrm{diag}\,(\lambda_1(R), \lambda_2(R), 1)$). With the obtained elastic strain tensor, the local value of the stress tensor can be derived from the neo-Hookean constitutive relation, which is then output for finite element calculations. To simulate the processes of growth-induced deformations, the growth functions $\lambda_1(R)$ and $\lambda_1(R)$ are selected as the controlling parameters, which vary linearly from 1 to the specified values during the whole simulation processes. The material constants in the model are chosen such that the Poisson's ratio $\nu = 0.4995$ (close to the incompressibility condition). The three samples of $2h = 0.001$, 0.05 and 0.1 are meshed into 64000, 50000 and 25000 CAX4H (4-node bilinear axisymmetric quadrilateral hybrid) elements, respectively. To capture the out-of-plane bending deformations of the plate, the first linear buckling mode multiplied by a damping factor is incorporated as the initial geometric imperfection of

the plate.

The obtained numerical results are shown in Fig. 2, which are also compared with the analytical results given in (17)-(19). It can be seen that the analytical results and the numerical results match well with each other, only except a small deviation observed from the case 1-2 ($2h = 0.1$) shown in Fig. 2E. Thus, the accuracy of the solution (16) can be verified. For the case 1-2 with $2h = 0.1$, the deviation should be partly due to the relatively large value of h, which could yield a large error of the analytical solution derived from the asymptotic method. Besides that, we found that corresponding to the growth functions given in (18), the quantity Δ changes from 0.040 to 1.958 when R increases from 0.2 to 1.2, which implies that the plate will undergo a significant bending deformation (cf. the solution given in (18)). Accompanying the bending deformation, some internal stresses will be activated in the plate, which possess the magnitudes of $O(h)$. However, with the analytical solution (16), we can only determine the leading-order terms the stress components, which may possess differences with the practical stress distribution in the plate. Therefore, the accuracy of the predicted deformations of the plate will also be influenced.

3.2. In-plane flat deformation

Besides the out-of-plane bending deformation, the plate can also undergo the in-plane flat deformation with any given growth functions $\{\lambda_1, \lambda_2\}$, which corresponds to the case $z_{0,R}^{(0)} = 0$. In this case, the leading-order terms in the plate equation $(12)_2$ are set equal to zero and the only non-trivial boundary condition in Eq. (10) is given by

$$\bar{S}_{Rr} = S_{Rr}^{(0)} + hS_{Rr}^{(1)}\Big|_{R=R_0,R_1} = 0. \tag{20}$$

Next, we need to solve the plate equations (12) subject to the boundary conditions (20), such that the flat deformation of the plate can be described. Since the exact solution of this equation system is difficult to be obtained, here we adopt a nonlinear perturbation method to derive the asymptotic solution.

First, from Eq. (16), we found that if the growth functions satisfy $\lambda_1 = F_{,R} = \lambda_2 + R\lambda_{2,R}$, the plate will undergo the flat deformation with the position field $r^{(0)} = F(R)$ and $z_{,R}^{(0)} = 0$. This result provides the fundamental solution for the perturbation method. In more general cases, we suppose the growth
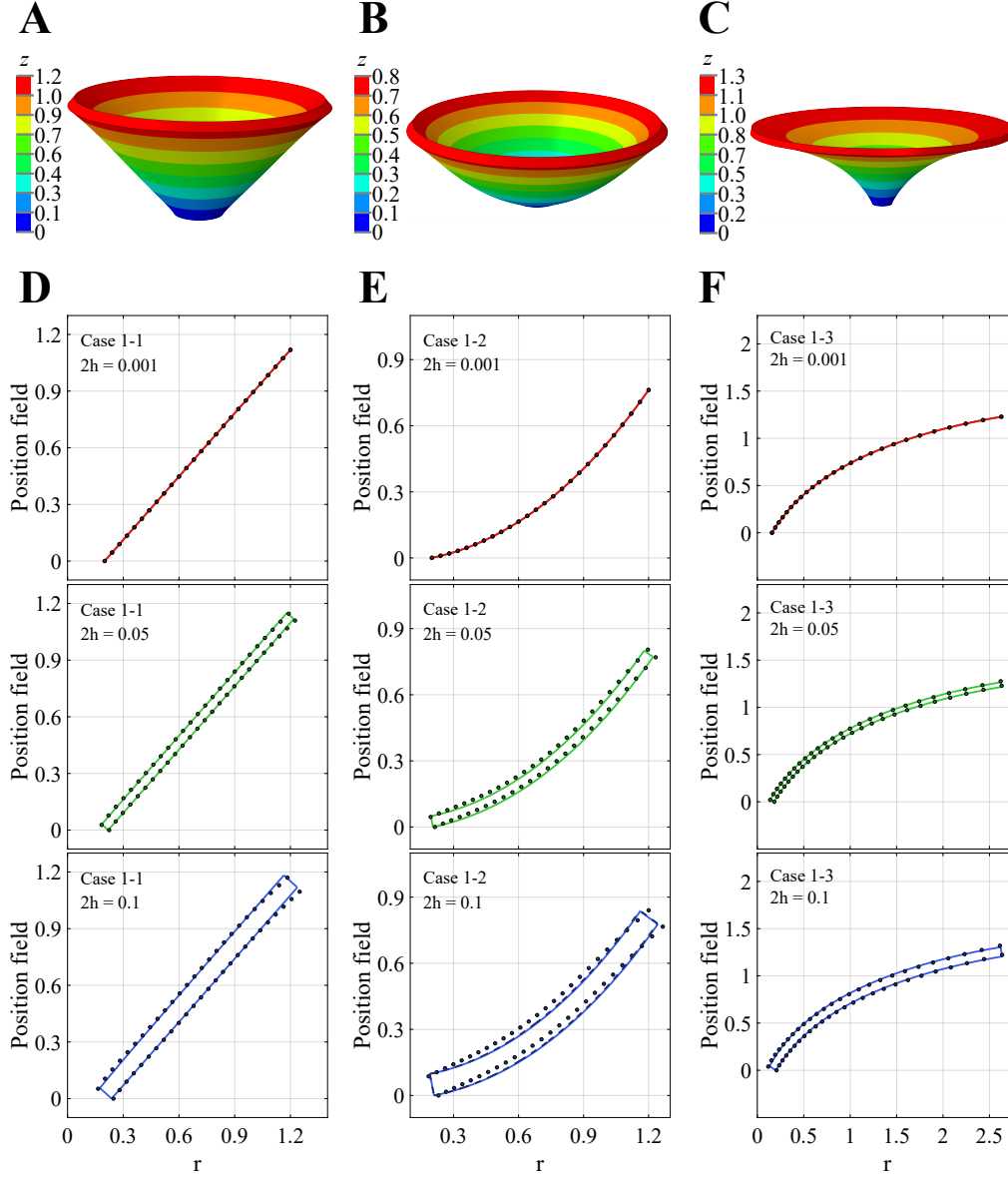
Figure 2: Axisymmetric bending deformation of a circular hyperelastic plate (inner radius $R_0 = 0.2$, outer radius $R_1 = 1.2$, thickness $2h = 0.001$, 0.05 and 0.1) induced by the growth functions given in Eqs. (17)-(19). Numerical simulation results of the current configurations of the plate with $2h = 0.1$: (A) case 1-1; (B) case 1-2; (C) case 1-3. Comparisons of the position fields $\{r, z\}$ obtained from the analytical results (solid lines) and the numerical results (dots): (D) case 1-1; (E) case 1-2; (F) case 1-3.

14

functions satisfy the following relation

$$\lambda_1 = F_{,R}\left(1 + \epsilon\delta\lambda\right),\tag{21}$$

where ϵ is a perturbation parameter and $\delta\lambda$ is the associated variational function. Corresponding to (21) and based on the fundamental solution, the asymptotic solution can be written as

$$r^{(0)} = F\left[1 + \left(\epsilon\delta U_1^{(0)} + \epsilon^2\delta U_2^{(0)} + \epsilon^3\delta U_3^{(0)}\right)\right.$$
$$\left. + h\left(\epsilon\delta U_1^{(1)} + \epsilon^2\delta U_2^{(1)} + \epsilon^3\delta U_3^{(1)}\right) + O(h^2)\right],\tag{22}$$
$$z_{,R}^{(0)} = h\left(\epsilon\delta W_1^{(1)} + \epsilon^2\delta W_2^{(1)}\right) + O(h^2)$$

where $\delta U_1^{(0)}$-$\delta U_3^{(0)}$, $\delta U_1^{(1)}$-$\delta U_3^{(1)}$ and $\delta W_1^{(1)}$-$\delta W_2^{(1)}$ are eight unknowns to be determined.

By substituting (21) and (22) into the plate equation $(12)_1$ and considering the terms of $O(h^m\epsilon^n)$ $(m = 0, 1;\ n = 1, 2, 3)$, we obtain

$$\delta U_{1,RR}^{(m)} + \delta U_{1,R}^{(m)}\left(\frac{3F_{,R}}{F} - \frac{F_{,RR}}{F_{,R}}\right) + \mathcal{F}_1^{(m)}(F, \delta\lambda) = 0,\tag{23$_1$}$$

$$\delta U_{2,RR}^{(m)} + \delta U_{2,R}^{(m)}\left(\frac{3F_{,R}}{F} - \frac{F_{,RR}}{F_{,R}}\right) + \mathcal{F}_2^{(m)}(F, \delta\lambda, \delta U_1^{(k)}) = 0,\tag{23$_2$}$$

$$\delta U_{3,RR}^{(m)} + \delta U_{3,R}^{(m)}\left(\frac{3F_{,R}}{F} - \frac{F_{,RR}}{F_{,R}}\right) + \mathcal{F}_3^{(m)}(F, \delta\lambda, \delta U_1^{(k)}, \delta U_2^{(k)}) = 0,\tag{23$_3$}$$

where $k = 0,\ 1$, and the explicit expressions of $\mathcal{F}_n^{(m)}$ are presented in Appendix B. Eqs. $(23)_1$-$(23)_3$ can be solved successively, from which we obtain the following solutions

$$\delta U_n^{(m)} = c_{n,1}^{(m)} + c_{n,2}^{(m)}\int_{R_0}^{R}\frac{F_{,R}(\tau)}{F(\tau)^3}\mathrm{d}\tau + \int_{R_0}^{R}\frac{\mathcal{L}_n^{(m)}(\tau)F_{,R}(\tau)}{F(\tau)^3}\mathrm{d}\tau,\tag{24}$$

where $\mathcal{L}_n^{(m)}(\tau) = \int_{R_0}^{\tau} -F(\tau_1)^3\mathcal{F}_n^{(m)}(\tau_1)/F_{,R}(\tau_1)\mathrm{d}\tau_1$, and $c_{n,1}^{(m)}$ and $c_{n,2}^{(m)}$ $(m = 0, 1;\ n = 1, 2, 3)$ are some integration constants. By further substituting (21) and (22) into the plate equation $(12)_2$ and comparing the coefficients of $h\epsilon^n$ $(n = 2, 3)$, we have another two equations

$$2F\delta W_1^{(1)} - F_{,R}\delta\lambda = 0,$$
$$F^2\delta U_{1,R}^{(0)\,2} + 2FF_{,R}\left(\delta\lambda\delta U_{1,R}^{(0)} - 2\delta W_2^{(1)}\right) + F_{,R}^{\,2}\delta\lambda\left(5\delta U_1^{(0)} - 3\delta\lambda\right) = 0.\tag{25}$$

These two equations can be solved explicitly and we obtain

$$\delta W_1^{(1)} = \frac{\delta \lambda F_{,R}}{2F},$$

$$\delta W_2^{(1)} = \frac{\delta \lambda \delta U_{11,R}^{(0)}}{2} + \frac{F \delta U_{11,R}^{(0)^2}}{2F_{,R}} + \frac{F_{,R} \delta \lambda}{2F} \left(5\delta U_1^{(0)} - 3\delta \lambda \right). \tag{26}$$

The constants $c_{n,1}^{(m)}$ and $c_{n,2}^{(m)}$ ($m = 0, 1$; $n = 1, 2, 3$) in the solution (24) can be determined from the boundary conditions (20), where we need to set the terms of $O(h^m \epsilon^n)$ ($m = 0, 1$; $n = 1, 2, 3$) in $\bar{S}_{Rr}$ equal to zero. The lengthy expressions of these constants are omitted here for brevity. By substituting (24) and (26) into (22), we obtain the asymptotic expressions $r^{(0)}$ and $z^{(0)}$. By further using the relations (7), the asymptotic expressions of $r^{(1)}$ and $z^{(1)}$ can also be obtained. Then, the 3D configuration of the plate after the growth-induced deformation can be recovered.

To show the accuracy of the asymptotic solution, we still choose the three circular hyperelastic plates introduced in the previous subsection. The growth functions given in (17)-(19) are also adopted (where the quantity $\Delta > 0$ in the region of $[R_0, R_1]$). Corresponding to these growth functions, the position fields $r^{(0)}$ and $z^{(0)}$ in the plates are determined from Eqs. (22), (24) and (26), based on which the 3D configurations of the plates are also recovered. For the purpose of comparison, we also conduct finite element simulations on the flat deformations of the 3D hyperelastic plates, where the settings of the numerical calculations are same as those introduced in the previous subsection. In Fig. 3, we show the results of the distributions of radial position $r^{(0)}$ and the variations of thickness $\Delta z = z|_{Z=2h} - z|_{Z=0}$ of the plates in the three cases. It can be seen that the analytical results and the numerical results show good agreements, only except that some small derivations near the inner side $R = 0.2$ of the plate can be observed in the case 1-3 with $2h = 0.05$ and 0.1.

From Fig. 3, some features of the in-plane flat deformations of the hyperelastic plates can be revealed. For example, the curves of the radial position $r^{(0)}$ obtained from the different plates are almost overlapped, which implies that the thickness of the plate has insignificant influence on the radial displacement. Besides that, although the plates undergo in-plane flat deformations in these examples, it can be found that the thicknesses of the plates are not uniform along the radial direction. This feature is well captured by our analytical results.
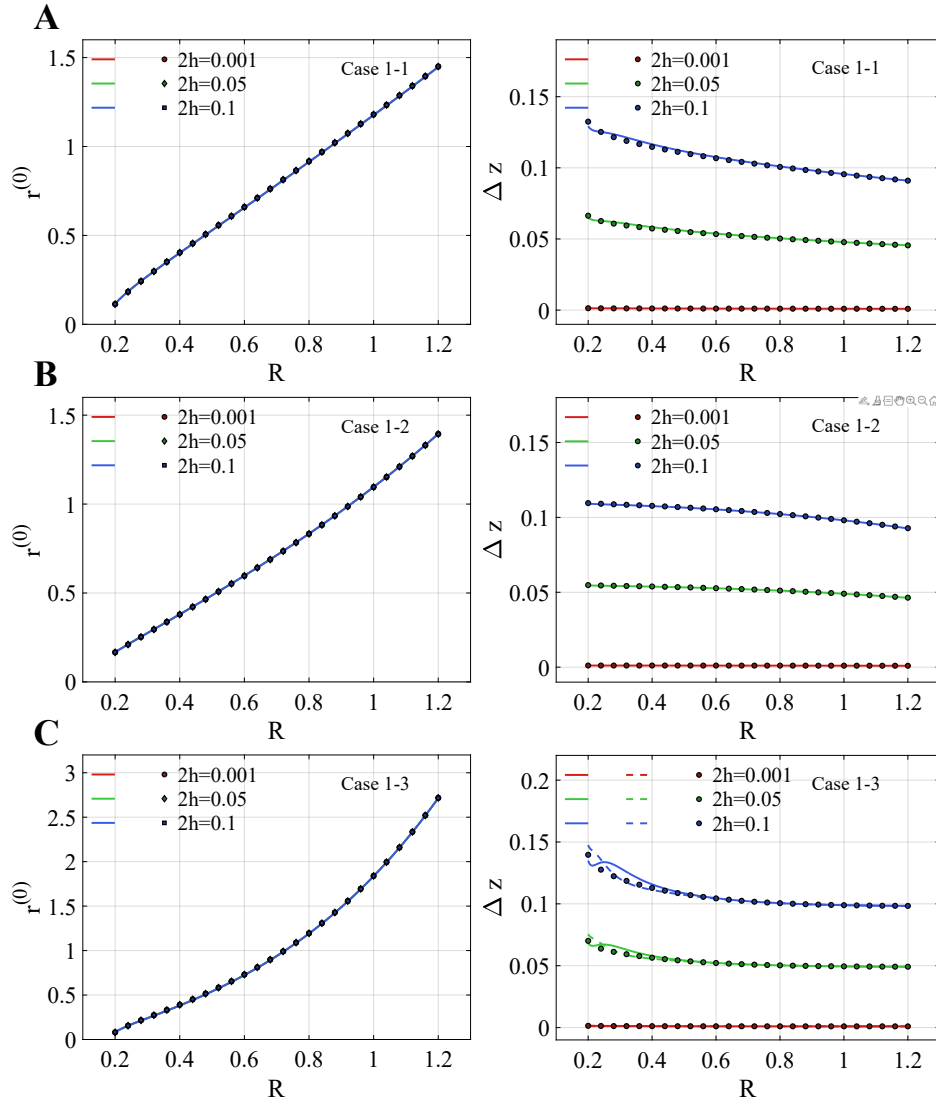
16

Figure 3: Axisymmetric flat deformation of a circular hyperelastic plate (inner radius $R_0 = 0.2$, outer radius $R_1 = 1.2$, thickness $2h = 0.001, 0.05$ and 0.1) induced by the growth functions given in Eqs. (19)-(21). $r^{(0)}$ and thickness $\Delta z = z|_{Z=2h} - z|_{Z=0}$ obtained from the analytical results (solid lines) and the numerical results (dots): (A) case 1-1; (B) case 1-2; (C) case 1-3.
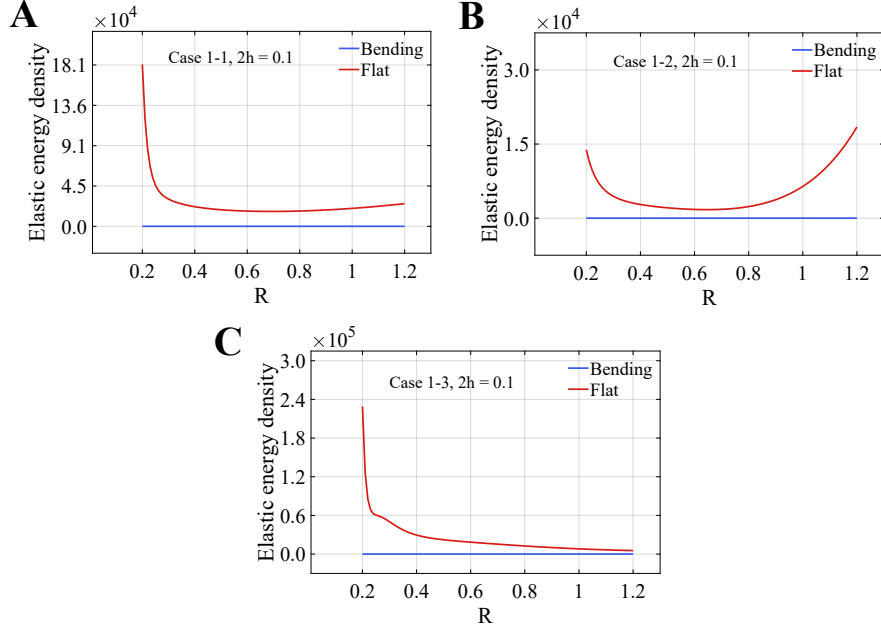
Figure 4: The elastic energy densities $\frac{1}{2h}\int_0^{2h}\phi dZ$ of the plate with $2h = 0.1, C_0 = 151136$ obtained from the flat and bending deformations: (A) case 1-1; (B) case 1-2; (C) case 1-3.

From the previous analyses, we have found that when $\Delta > 0$ in the region $[r_0, r_1]$, the plate may undergo both bending and flat deformations. Therefore, we need to study which solution would be the preferred one. In Fig. 3, the distributions of elastic energy densities corresponding to the bending and flat deformations of the hyperelastic plates are presented. It can be seen that the elastic energies of the plates obtained from the flat deformations are relatively large, while those of the bending deformations are almost equal to zero. Thus, from the viewpoint of energy, the bending deformation would be the preferred deformation style of the plates. If the growth functions satisfy $\Delta \leq 0$ in the region $[R_0, R_1]$, the analytical solution corresponding to the bending deformation does not exist (cf. Eq. (16)), thus the plate can only undergo the flat deformation.

Remarks:

- When the absolute value of Δ is large, the term $\epsilon\delta\lambda$ would also be large compared with 1. In this case, the accuracy of the asymptotic solution may not be good. For example, corresponding to the case 1-3 shown in Fig. 3, the value of $\epsilon\delta\lambda$ exceeds 0.8 near the inner side $R = 0.2$

18

of the plate, thus the asymptotic solution exhibits obvious differences from the numerical solutions when $2h = 0.05$ and 0.1. To improve the accuracy of the asymptotic solution, the terms with higher asymptotic orders should be adopted in Eq. (22).

- As we only consider the case of axisymmetric deformation, the plate keeps flat when $\Delta < 0$. If the restriction of axisymmetric deformation is removed, the plate may undergo wrinkling deformations when $\Delta < 0$.

3.3. Combined deformation

In the previous subsections, we have derived the analytical results for both bending and flat deformations of the circular hyperelastic plate. It was found that the type of deformation highly depends on the value of quantity Δ. If $\Delta > 0$, the out-of-plane bending deformation (i.e., $z_{0,R}^{(0)} \neq 0$) is preferred to take place since it has a lower energy value, while if $\Delta \leq 0$, the plate can only undergo the in-plane flat deformation (i.e., $z_{0,R}^{(0)} = 0$).

Sometimes, we may have $\Delta > 0$ in certain subregion and $\Delta \leq 0$ in the other subregion of the plate. In this case, the plate will undergo combined bending-flat deformations. Based on the previous analyses, we know that the deformation of the plate should satisfy the following conditions:

- $\Delta \leq 0$ in $[R_0', R_1'] \subseteq [R_0, R_1] \Rightarrow z_{0,R}^{(0)} = 0$ in $[R_0', R_1']$.

- $z_{0,R}^{(0)} \neq 0$ in $[R_0', R_1'] \subseteq [R_0, R_1] \Rightarrow \Delta > 0$ in $[R_0', R_1']$.

To describe the combined bending-flat deformation of the plate, both of the analytical solutions given in Eqs. (16) and (22) need to be adopted. In addition to the traction-free boundary condition (10), one also needs to propose suitable connecting conditions at the intersection positions of the different subregions. For the ease of explanation, we consider the illustration shown in Fig. 5, where $\Delta \leq 0$ in the inner part $[R_0, R']$ and $\Delta > 0$ in the outer part $[R', R_1]$ of the plate. From the two conditions introduced above, we can suppose that the plate undergoes the flat deformation (i.e., $z_{0,R}^{(0)} = 0$) in the inner subregion $[R_0, R^*]$ and the bending deformation (i.e., $z_{0,R}^{(0)} \geq 0$) in the outer subregion $[R^*, R_1]$, where $R^* > R'$. In fact, R' can be identified once the growth functions $\{\lambda_1, \lambda_2\}$ are given, but R^* can only be determined by solving the plate equations. We propose the following connection conditions proposed at the intersection position $R = R^*$

$$r_-|_{Z=2h} = r_+|_{Z=2h}, \quad z_-|_{Z=2h} = z_+|_{Z=2h}, \quad \bar{S}_{Rr,-} = \bar{S}_{Rr,+} = 0, \qquad (27)$$

19

which represent the continuities of the displacements and the radial stress component. For any given value of R^*, the analytical solutions in both the flat and bending deformation regions can be written out according to Eqs. (16) and (22), which already satisfy the connection condition $(27)_3$. From $(27)_1$, the exact value of R^* can be determined. Then, $(27)_2$ will be used to determine the shifts of the different parts of the plate along the Z-axis. Although here we only consider the simple example shown in Fig. 5, this solution scheme can be applied in more general cases of combined deformations.
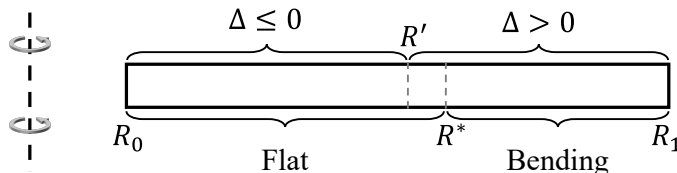

Figure 5: Illustration of the combined flat-bending deformation of a circular hyperelastic plate (only one section of the plate along the radial direction is shown).

To demonstrate the efficiency and the limit of the current analytical approach, some typical examples will be introduced below. We still consider the three circular hyperelastic plates adopted in the previous subsections. The following growth functions are selected to generate the combined bending-flat deformations of the plates

$$\lambda_1 = \frac{2}{5} + \frac{5R}{2}, \quad \lambda_2 = 2, \tag{28}$$

which correspond to the case $\Delta \leq 0$ when $0.2 \leq R \leq 0.64$ and $\Delta > 0$ when $0.64 < R \leq 1.2$. By using the scheme introduced above, the analytical solutions corresponding to this set of growth functions can be derived. For the purpose of comparison, we also conduct numerical simulations on the combined deformations of the 3D plate samples with the same growth functions. The simulated configurations of the plate and the comparisons between the analytical and numerical results are shown in Fig. 6.

From Fig. 6, it can be seen that the analytical results still provide good predictions on the combined bending-flat deformations of the plates. However, when the plate becomes thicker (e.g., $2h = 0.1$), some differences between the analytical and numerical results can be found during the neighboring region of R^*. The variations of the numerical solutions from the flat
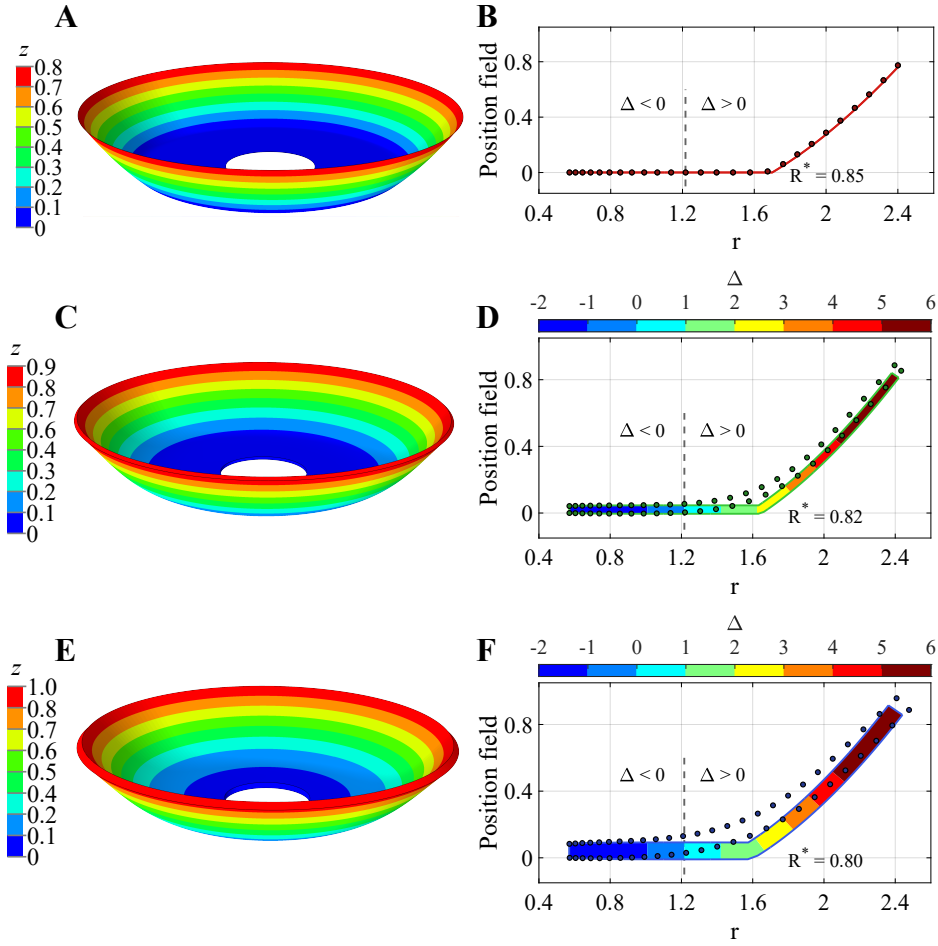
Figure 6: Combined bending-flat deformations of circular hyperelastic plates (inner radius $R_0 = 0.2$, outer radius $R_1 = 1.2$, thickness $2h = 0.001$, 0.05 and 0.1) induced by the growth functions given in Eq. (28). Simulated current configurations of the plate samples: (A) $2h = 0.001$; (C) $2h = 0.05$; (E) $2h = 0.1$. Comparisons of the position fields $\{r, z\}$ obtained from the analytical results (solid lines) and the numerical results (dots): (B) $2h = 0.001$, $R^* = 0.85$; (D) $2h = 0.05$, $R^* = 0.82$; (F) $2h = 0.1$, $R^* = 0.80$.

deformation region to the bending deformation region seem to be smoother than those of the analytical solutions. In our opinion, these differences should be partly attributed to the boundary layer effect. To improve the accuracy of the analytical results, some singular perturbation method should be adopted to solve the plate equation system. This problem deserves to be further investigated in the future.

4. Shape-control of circular hyperelastic plates

In the previous section, we have studied the problem of growth-induced axisymmetric deformation in a circular hyperelastic plate, where the growth functions have been specified in advance. Next, we study an inverse problem. That is, to achieve certain axisymmetric configuration, what kinds of growth functions should be set in the plate? This inverse problem is referred to as 'shape-programming/shape-control'. Here, we assume that the plate is sufficiently thin and the target configuration is only achieved by the bottom surface of the plate.
Remark: In the current modeling work, shape-control is just referred to the determination of the growth fields in the plate. While, how to generate these growth fields physically are not involved in this work. In experiments, differential growth (or expansion) of hyperelastic plates may be achieved by controlling the swelling ratio, temperature change or other physical fields in the plates (Ionov, 2013; Kempaiah and Nie, 2014; Liu et al., 2016; Siéfert et al., 2019).

It should be pointed out that the solution of the problem of shape-control may not be unique, because the same configuration of the plate can be generated from different growth functions. For simplicity, we always choose the growth functions such that $\Delta \geq 0$ in the whole plate region $[R_0, R_1]$ and only the leading-order terms of the position fields $\{r_0^{(0)}, z_0^{(0)}\}$ are considered. In this case, Eq. (15) holds, thus the following formula can be easily derived

$$\begin{cases} \lambda_1 = \sqrt{r_{0,R}^{(0)\,2} + z_{0,R}^{(0)\,2}}, \\ \lambda_2 = r^{(0)}/R. \end{cases} \tag{29}$$

Despite the simplicity of this formula, it enables us to design arbitrary axisymmetric configurations of the plate through growth. Another benefit of this formula is that in the generated configurations, the residual stress and

22

the elastic energy density are almost equal to zero (suppose the plate is sufficiently thin). Thus, the generated configurations of the plate would have good stability, which is an important feature for practical applications.

To verify the efficiency of formula (29) for shape-control, some illustrative examples are presented in Fig. 7 (also see Movie 1 for the illustrations of the growing processes). In these examples, the reference configuration of the circular plate still has the inner radius $R_0 = 0.2$ and outer radius $R_1 = 1.2$. The thickness of the plate is set to be $2h = 0.001$. Corresponding to the different target configurations (which mimic the shapes of a basketball, an American football, an Ipomoea cairica, a Nymphaea nouchali var. caerulea, a Lagenaria siceraria, and a jellyfish), the position fields $\{r_0^{(0)}, z_0^{(0)}\}$ in the plate are first specified, then the growth functions $\{\lambda_1, \lambda_2\}$ are calculated by using Eq. (29) (the explicit expressions of $\{r_0^{(0)}, z_0^{(0)}\}$ and $\{\lambda_1, \lambda_2\}$ can be found in the Appendix C). To verify the accuracy of the analytical results, we also conduct numerical simulations with the 3D plate sample. The simulation results are shown in Fig. 7. Comparisons between the target and the simulated position fields in plate have also been given in Fig. 7, which show very good consistency. It should be noted that in the examples shown in Fig. 7, we just aim to mimic the geometrical shapes of the different biological bodies, but not to reveal the underlying mechanisms of biological growth in the different cases. Besides that, some detailed features of the biological bodies cannot be captured by our modeling results, e.g., the long wavelength wrinkles on the Ipomoea cairica (cf. Fig. 7C), the kinks on the vertical walls of the Nymphaea nouchali var. caerulea (cf. Fig. 7D).

5. Conclusions

In this work, we investigated the growth-induced axisymmetric deformations of thin circular hyperelastic plates. The following results have been obtained: (1) a consistent finite-strain plate equation system containing growth parameters is formulated, which lays the foundation for the current work; (2) the plate equations were solved analytically and the obtained solutions can provide accurate predictions on the growth-induced deformations of the plate; (3) a criterion is set up such that the types of deformations (i.e., out-of-plane bending deformation or in-plane flat deformation) of the plate can be determined with any given growth functions; (4) by studying an inverse problem, some analytical formulas are derived for the shape-control of the plate, from
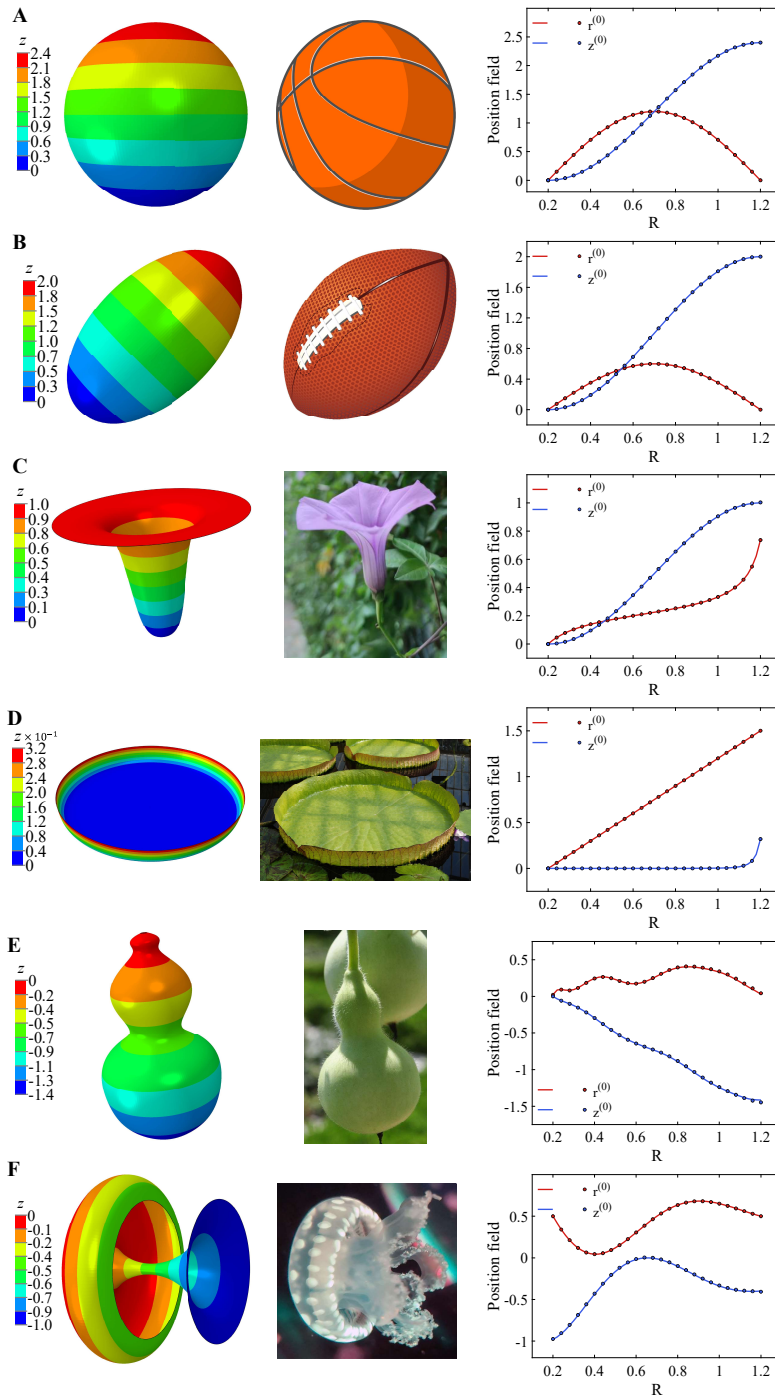
Figure 7: Some illustrative examples for shape-control of a circular hyperelastic plate and comparisons of the position fields $\{r_0^{(0)}, z_0^{(0)}\}$ obtained from the analytical results (solid lines) and the numerical results (dots, taken from the bottom line $\{\Theta = 0, Z = 0, R_0 \leq R \leq R_1\}$ of the plate) : (A) a basketball; (B) an American football; (C) an Ipomoea cairica; (D) a Victoria amazonica; (E) a Lagenaria siceraria; (F) a Phyllorhiza punctata.

24

which the growth functions corresponding to most 3D axisymmetric configurations can be identified.

The analytical results obtained in the present work can provide important insight into the effects of growth on the deformation features of thin circular hyperelastic plates, which have wide potential applications in the engineering fields. However, it should also be noted that the analytical results are derived based on some idealized assumptions, e.g., the free growth condition and the axisymmetric deformation of the plates. To fulfill the requirements of practical applications, the problems with more general boundary conditions and deformation styles need to be investigated in the future.

Supplementary material

Movie 1: Growth process of shape-control cases. Video of the growing processes of the six illustrative examples introduced in Fig. 7 of the main text.

Data Availability

The data sheets of the numerical results are available at https://github.com/Jeff97/Data-for-deformation-of-circular-plate.

Appendix A. Expressions of some stress components

In cylindrical coordinate system, the components of leading-order stress tensor $\mathbb{S}^{(0)}$ in $(6)_3$ are given by

$$S_{Rr}^{(0)} = -\frac{p^{(0)}r^{(0)}}{R}z^{(1)} + \frac{2C_0\lambda_2}{\lambda_1}r_{,R}^{(0)},$$

$$S_{Rz}^{(0)} = \frac{p^{(0)}r^{(0)}}{R}r^{(1)} + \frac{2C_0\lambda_2}{\lambda_1}z_{,R}^{(0)},$$

$$S_{\Theta\theta}^{(0)} = p^{(0)}\left(r^{(1)}z_{,R}^{(0)} - z^{(1)}r_{,R}^{(0)}\right) + \frac{2C_0\lambda_1}{R\lambda_2}r^{(0)},$$

$$S_{Zr}^{(0)} = \frac{p^{(0)}r^{(0)}}{R}z_{,R}^{(0)} + 2C_0\lambda_1\lambda_2 r^{(1)},$$

$$S_{Zz}^{(0)} = -\frac{p^{(0)}r^{(0)}}{R}r_{,R}^{(0)} + 2C_0\lambda_1\lambda_2 z^{(1)},$$

$$S_{R\theta}^{(0)} = S_{\Theta r}^{(0)} = S_{\Theta z}^{(0)} = S_{Z\theta}^{(0)} = 0.$$

Under the assumption of axisymmetric deformation and by substituting the expressions of $r^{(1)}$-$r^{(2)}$, $z^{(1)}$-$z^{(2)}$ and $p^{(0)}$-$p^{(1)}$, the stress components $S_{Rr}^{(1)}$,

26

$S_{\Theta\theta}^{(1)}$ and $S_{Rz}^{(1)}$ given in Eq. (12) can be written as

$$S_{Rr}^{(1)} = -\frac{2C_0}{Rr^{(0)^4}\lambda_1\left(r_{,R}^{(0)^2} + z_{,R}^{(0)^2}\right)^4}\left\{-R^4\lambda_1{}^5\lambda_2{}^4 r_{,R}^{(0)} z_{,R}^{(0)}\left(r_{,R}^{(0)^2} + z_{,R}^{(0)^2}\right)\right.$$

$$+ 2r^{(0)^4}\lambda_1{}^3 r_{,R}^{(0)} z_{,R}^{(0)}\left(r_{,R}^{(0)^2} + z_{,R}^{(0)^2}\right)^2 - R^2 r^{(0)^2}\lambda_1\lambda_2{}^2 r_{,R}^{(0)} z_{,R}^{(0)}\left(r_{,R}^{(0)^2} + z_{,R}^{(0)^2}\right)^3$$

$$+ 2R^2 r^{(0)^3}\lambda_2{}^2\left(r_{,R}^{(0)^2} + z_{,R}^{(0)^2}\right)^2\left[z_{,R}^{(0)}\left(\left(r_{,R}^{(0)^2} + z_{,R}^{(0)^2}\right)\lambda_{1,R} - 2\lambda_1 r_{,R}^{(0)} r_{,RR}^{(0)}\right)\right.$$

$$\left. + \lambda_1\left(r_{,R}^{(0)^2} - z_{,R}^{(0)^2}\right)z_{,RR}^{(0)}\right] + 2R^3 r^{(0)}\lambda_1{}^4\lambda_2{}^3\left[z_{,R}^{(0)}\left[\left(r_{,R}^{(0)^2} + z_{,R}^{(0)^2}\right)\left(R\lambda_2\lambda_{1,R}\right.\right.\right.$$

$$\left.\left. + \lambda_1\left(\lambda_2 + R\lambda_{2,R}\right)\right) - 2R\lambda_1\lambda_2 r_{,R}^{(0)} r_{,RR}^{(0)}\right] + R\lambda_1\lambda_2\left(r_{,R}^{(0)^2} - z_{,R}^{(0)^2}\right)z_{,RR}^{(0)}\right]\bigg\},$$

$$S_{\Theta\theta}^{(1)} = -\frac{2C_0}{r^{(0)^5}\left(r_{,R}^{(0)^2} + z_{,R}^{(0)^2}\right)^3}\left\{2r^{(0)^4}\lambda_1{}^2 z_{,R}^{(0)}\left(r_{,R}^{(0)^2} + z_{,R}^{(0)^2}\right)^2 + R^2 r^{(0)^3}\lambda_2{}^2\right.$$

$$\left(r_{,R}^{(0)^2} + z_{,R}^{(0)^2}\right)^2\left(-z_{,R}^{(0)} r_{,RR}^{(0)} + r_{,R}^{(0)} z_{,RR}^{(0)}\right) + R^4\lambda_1{}^4\lambda_2{}^4\left[z_{,R}^{(0)}\left(2\left(r_{,R}^{(0)^2} + z_{,R}^{(0)^2}\right)\right.\right.$$

$$\left.\left.- r^{(0)} r_{,RR}^{(0)}\right) + r^{(0)} r_{,R}^{(0)} z_{,RR}^{(0)}\right]\bigg\},$$

$$S_{Rz}^{(1)} = -\frac{2C_0}{Rr^{(0)^4}\lambda_1\left(r_{,R}^{(0)^2} + z_{,R}^{(0)^2}\right)^4}\left\{-r^{(0)^4}\lambda_1{}^3\left(r_{,R}^{(0)^2} - z_{,R}^{(0)^2}\right)\left(r_{,R}^{(0)^2} + z_{,R}^{(0)^2}\right)^2\right.$$

$$+ R^2 r^{(0)^2}\lambda_1\lambda_2{}^2 r_{,R}^{(0)^2}\left(r_{,R}^{(0)^2} + z_{,R}^{(0)^2}\right)^3 + R^4\lambda_1{}^5\lambda_2{}^4\left(r_{,R}^{(0)^2} + z_{,R}^{(0)^2}\right)$$

$$\times\left(2r_{,R}^{(0)^2} + z_{,R}^{(0)^2}\right) - 2R^2 r^{(0)^3}\lambda_2{}^2\left(r_{,R}^{(0)^2} + z_{,R}^{(0)^2}\right)^2\left[r_{,R}^{(0)^3}\lambda_{1,R} - \lambda_1 r_{,R}^{(0)^2} r_{,RR}^{(0)}\right.$$

$$\left. + \lambda_1 z_{,R}^{(0)^2} r_{,RR}^{(0)} + r_{,R}^{(0)} z_{,R}^{(0)}\left(z_{,R}^{(0)}\lambda_{1,R} - 2\lambda_1 z_{,RR}^{(0)}\right)\right] - 2R^4 r^{(0)}\lambda_1{}^4\lambda_2{}^4 r_{,R}^{(0)}$$

$$\lambda_{1,R}\left(r_{,R}^{(0)^2} + z_{,R}^{(0)^2}\right) - 2R^3 r^{(0)}\lambda_1{}^5\lambda_2{}^3\left[Rr_{,R}^{(0)}\left(r_{,R}^{(0)^2} + z_{,R}^{(0)^2}\right)\lambda_{2,R}\right.$$

$$\left.\left. + \lambda_2\left(r_{,R}^{(0)^3} - Rr_{,R}^{(0)^2} r_{,RR}^{(0)} + Rz_{,R}^{(0)^2} r_{,RR}^{(0)} + r_{,R}^{(0)} z_{,R}^{(0)}\left(z_{,R}^{(0)} - 2Rz_{,RR}^{(0)}\right)\right)\right]\right\}.$$

27

Appendix B. Expressions of the terms $\mathcal{F}_n^{(m)}$

The expressions of the terms $\mathcal{F}_n^{(m)}$ $(m = 0, 1; n = 1, 2, 3)$ in Eq. (23) are given by

$$\mathcal{F}_1^{(0)} = -\frac{\delta\lambda_{,R}F_{,R}}{F} - \frac{\delta\lambda F_{,R}^2}{2F^2},$$

$$\mathcal{F}_2^{(0)} = \frac{1}{4F^2}\Big[F^2\delta U_{11,R}^{(0)}\left(3\delta U_{11,R}^{(0)} - 4\delta\lambda_{,R}\right) - 2FF_{,R}\Big(3\delta\lambda\delta U_{11,R}^{(0)}$$
$$+ 2\delta\lambda_{,R}\left(\delta U_{11}^{(0)} - \delta\lambda\right)\Big) + \delta\lambda F_{,R}^2\left(-11\delta U_{11}^{(0)} + 5\delta\lambda\right)\Big],$$

$$\mathcal{F}_3^{(0)} = \frac{1}{8}\bigg[4\delta U_{11,R}^{(0)}\left(3\delta U_{12,R}^{(0)} + 2\delta\lambda\delta\lambda_{,R}\right) - 15\delta U_{11}^{(0)}\delta U_{11,R}^{(0)\,2} - 8\delta U_{12,R}^{(0)}\delta\lambda_{,R}$$

$$- \frac{6F\delta U_{11,R}^{(0)\,3}}{F_{,R}} - \frac{2F_{,R}}{F}\bigg[-9\delta\lambda\delta U_{11,R}^{(0)}\left(-2\delta U_{11}^{(0)} + \delta\lambda\right)$$
$$+ 6\delta\lambda\delta U_{12,R}^{(0)} + 4\delta\lambda_{,R}\left(\delta U_{12}^{(0)} + \delta\lambda\left(-\delta U_{11}^{(0)} + \delta\lambda\right)\right)\bigg]$$

$$- \frac{\delta\lambda F_{,R}^2}{F^2}\left(36\delta U_{11}^{(0)\,2} + 22\delta U_{12}^{(0)} - 37\delta U_{11}^{(0)}\delta\lambda + 12\delta\lambda^2\right)\bigg],$$

$$\mathcal{F}_1^{(1)} = 0,$$

$$\mathcal{F}_2^{(1)} = \frac{1}{4F^2}\Big(2F^2\delta U_{11,R}^{(1)}\left(3\delta U_{11,R}^{(0)} - 2\delta\lambda_{,R}\right) - 2FF_{,R}\Big(3\delta\lambda\delta U_{11,R}^{(0)}$$
$$+ 2\delta U_{11}^{(1)}\delta\lambda_{,R}\Big) - 11\delta U_{11}^{(1)}\delta\lambda F_{,R}^2\Big),$$

$$\mathcal{F}_3^{(1)} = \frac{1}{8}\bigg[-15\delta U_{11}^{(1)}\delta U_{11,R}^{(0)\,2} + 6\delta U_{11,R}^{(1)}\left(-5\delta U_{11}^{(0)}\delta U_{11,R}^{(0)} + 2\delta U_{12,R}^{(0)}\right)$$

$$+ 12\delta U_{11,R}^{(0)}\delta U_{12,R}^{(1)} + 8\delta\lambda_{,R}\left(\delta\lambda\delta U_{11,R}^{(1)} - \delta U_{12,R}^{(1)}\right)$$

$$- \frac{2F_{,R}}{F}\bigg[3\delta\lambda\left(6\delta U_{11}^{(1)}\delta U_{11,R}^{(0)} + 3\delta U_{11,R}^{(1)}\left(2\delta U_{11}^{(0)} - \delta\lambda\right) + 2\delta U_{12,R}^{(1)}\right)$$

$$+ 4\delta\lambda_{,R}\left(\delta U_{12}^{(1)} - \delta U_{11}^{(1)}\delta\lambda\right)\bigg] - \frac{18F\delta U_{11,R}^{(0)\,2}\delta U_{11,R}^{(1)}}{F_{,R}} + \frac{\delta\lambda F_{,R}^2}{F^2}$$

$$\left(-72\delta U_{11}^{(0)}\delta U_{11}^{(1)} - 22\delta U_{12}^{(1)} + 37\delta U_{11}^{(1)}\delta\lambda\right)\bigg].$$

Appendix C. Position fields and growth functions for shape-control

The position fields and growth functions of the six examples of shape-control presented in Fig. 7 are given below

- Case 3-1 (Basketball):

$$
\begin{cases}
\lambda_1 = \dfrac{6\pi}{5}, \\[2mm]
\lambda_2 = \dfrac{6}{5R} \sin\left(\pi R - \dfrac{\pi}{5}\right), \\[2mm]
r^{(0)} = \dfrac{6}{5} \sin\left(\pi R - \dfrac{\pi}{5}\right), \\[2mm]
z^{(0)} = \dfrac{6}{5} - \dfrac{6}{5} \cos\left(\pi R - \dfrac{\pi}{5}\right).
\end{cases}
$$

- Case 3-2 (American football):

$$
\begin{cases}
\lambda_1 = \dfrac{\pi}{5} \sqrt{17 - 8\cos\left(2\pi R - \dfrac{2\pi}{5}\right)}, \\[2mm]
\lambda_2 = \dfrac{3}{5R} \sin\left(\pi R - \dfrac{\pi}{5}\right), \\[2mm]
r^{(0)} = \dfrac{3}{5} \sin\left(\pi R - \dfrac{\pi}{5}\right), \\[2mm]
z^{(0)} = 1 - \cos\left(\pi R - \dfrac{\pi}{5}\right).
\end{cases}
$$

- Case 3-3 (Ipomoea cairica):

$$
\begin{cases}
\lambda_1 = \dfrac{\pi}{50} \sqrt{625\sin^2\left(\pi R - \dfrac{\pi}{5}\right) + 16\sec^4\left(\dfrac{4\pi R}{5} - \dfrac{42\pi}{400}\right)}, \\[2mm]
\lambda_2 = \dfrac{1}{10R} \left[\tan\left(\dfrac{4\pi R}{5} - \dfrac{42\pi}{400}\right) + \cot\dfrac{7\pi}{50}\right], \\[2mm]
r^{(0)} = \dfrac{1}{10} \left[\tan\left(\dfrac{4\pi R}{5} - \dfrac{42\pi}{400}\right) + \cot\dfrac{7\pi}{50}\right], \\[2mm]
z^{(0)} = \sin^2\left(\dfrac{\pi R}{2} - \dfrac{\pi}{10}\right).
\end{cases}
$$

- Case 3-4 (Nymphaea nouchali var. caerulea):

$$
\begin{cases}
\lambda_1 = \sqrt{\dfrac{81R^{16}}{40000}e^{2(R^9-1)} + \dfrac{9}{4}}, \\[2ex]
\lambda_2 = \dfrac{3}{2R}\left(R - \dfrac{1}{5}\right), \\[2ex]
r^{(0)} = \dfrac{3}{2}\left(R - \dfrac{1}{5}\right), \\[2ex]
7z^{(0)} = \dfrac{1}{200}e^{\left(R^9-1\right)} - 0.001839.
\end{cases}
$$

- Case 3-5 (Lagenaria siceraria):

$$
\begin{cases}
\lambda_1 = \sqrt{A^2 + B^2}, \\[1ex]
\lambda_2 = \dfrac{C}{R}, \\[1ex]
\begin{aligned}
A =\ & 55337.5R^7 - 221000R^6 + 244017R^5 - 66950.8R^3 \\
& + 7139.21R^2 - 33549.3R + 21712.8\sin(2.61799R) \\
& - 4662.35\sin(5.23599R) - 20.4042\sin(10.472R) + 96.3201,
\end{aligned} \\
\begin{aligned}
B =\ & 83489.8R^7 - 398726R^6 + 516652R^5 + 292433R^3 \\
& - 1.01094 \times 10^6 R^2 + 14187.2R - 270078\cos(2.61799R) \\
& + 405.277\cos(5.23599R) - 33.4458\cos(10.472R) + 268790,
\end{aligned} \\
\begin{aligned}
C =\ & -10436.2R^8 + 56960.8R^7 - 86108.7R^6 - 73108.1R^4 \\
& + 336980R^3 - 7093.59R^2 - 268790R + 103162\sin(2.61799R) \\
& - 77.4023\sin(5.23599R) + 3.19384\sin(10.472R) - 49.2918,
\end{aligned} \\
r^{(0)} = C, \\
\begin{aligned}
z^{(0)} =\ & 7395.6 + 6917.19R^8 - 31571.4R^7 + 40669.4R^6 \\
& - 16737.7R^4 + 2379.74R^3 - 16774.7R^2 + 96.3201R \\
& - 8293.7\cos(2.61799R) + 890.444\cos(5.23599R) \\
& + 1.94846\cos(10.472R) - 0.0520998.
\end{aligned}
\end{cases}
$$

- Case 3-6 (Jellyfish):

$$
\begin{cases}
\lambda_1 = \dfrac{2}{\pi}\sqrt{\left(\dfrac{125}{809}\right)^{\frac{24R}{\pi}} 2^{\frac{48R}{\pi}} \left[\pi^4 + 36\log^2\left(\dfrac{809}{500}\right)\right]}, \\[4mm]
\lambda_2 = \dfrac{1}{R}\left[\left(\dfrac{809}{500}\right)^{-\frac{12R}{\pi}} \cos\left(2\pi R + \dfrac{\pi}{10}\right) + \dfrac{1}{2}\right], \\[4mm]
r^{(0)} = \left(\dfrac{809}{500}\right)^{-\frac{12R}{\pi}} \cos\left(2\pi R + \dfrac{\pi}{10}\right) + \dfrac{1}{2}, \\[4mm]
z^{(0)} = -\left(\dfrac{809}{500}\right)^{-\frac{12R}{\pi}} \sin\left(2\pi R + \dfrac{\pi}{10}\right) - 0.28811.
\end{cases}
$$

References

Abdullah, A. M., Li, X., Braun, P. V., Rogers, J. A., and Hsia, K. J. (2018). Self-folded gripper-like architectures from stimuli-responsive bilayers. *Advanced Materials*, 30(31):e1801669.

Ambrosi, D., Ben Amar, M., Cyron, C. J., DeSimone, A., Goriely, A., Humphrey, J. D., and Kuhl, E. (2019). Growth and remodelling of living tissues: perspectives, challenges and opportunities. *Journal of The Royal Society Interface*, 16(157):20190233.

Ben Amar, M. and Goriely, A. (2005). Growth and instability in elastic tissues. *Journal of the Mechanics and Physics of Solids*, 53(10):2284–2319.

Ben Amar, M., Nassoy, P., and LeGoff, L. (2019). Physics of growing biological tissues: the complex cross-talk between cell activity, growth and resistance. *Philosophical Transactions of the Royal Society A: Mathematical, Physical and Engineering Sciences*, 377(2144):20180070.

Budday, S., Steinmann, P., and Kuhl, E. (2014). The role of mechanics during brain development. *Journal of the Mechanics and Physics of Solids*, 72:75–92.

Chen, X., Ciarletta, P., and Dai, H.-H. (2021). Physical principles of morphogenesis in mushrooms. *Physical Review E*, 103:022412.

Chen, X. and Dai, H.-H. (2020). Stress-free configurations induced by a family of locally incompatible growth functions. *Journal of the Mechanics and Physics of Solids*, 137:103834.

Coen, E., Rolland-Lagan, A.-G., Matthews, M., Bangham, J. A., and Prusinkiewicz, P. (2004). The genetics of geometry. *Proceedings of the National Academy of Sciences of the United States of America*, 101(14):4728–4735.

Dai, H.-H. and Song, Z. (2014). On a consistent finite-strain plate theory based on three-dimensional energy principle. *Proceedings of the Royal Society A: Mathematical, Physical and Engineering Sciences*, 470(2171):20140494.

Dervaux, J., Ciarletta, P., and Ben Amar, M. (2009). Morphogenesis of thin hyperelastic plates: A constitutive theory of biological growth in the Föppl–von Kármán limit. *Journal of the Mechanics and Physics of Solids*, 57(3):458–471.

Dias, M., Hanna, J., and Santangelo, C. (2011). Programmed buckling by controlled lateral swelling in a thin elastic sheet. *Physical Review E*, 84:036603.

Du, P., Dai, H.-H., Wang, J., and Wang, Q. (2020). Analytical study on growth-induced bending deformations of multi-layered hyperelastic plates. *International Journal of Non-Linear Mechanics*, 119:103370.

Efrati, E., Sharon, E., and Kupferman, R. (2009a). Buckling transition and boundary layer in non-euclidean plates. *Physical Review E*, 80:016602.

Efrati, E., Sharon, E., and Kupferman, R. (2009b). Elastic theory of unconstrained non-euclidean plates. *Journal of the Mechanics and Physics of Solids*, 57(4):762–775.

Gladman, A. S., Matsumoto, E. A., Nuzzo, R. G., Mahadevan, L., and Lewis, J. A. (2016). Biomimetic 4d printing. *Nature Materials*, 15(4):413–418.

Goriely, A. (2017). *The mathematics and mechanics of biological growth*, volume 45. Springer.

Green, P. B. (1996). Transductions to generate plant form and pattern: an essay on cause and effect. *Annals of Botany*, 78(3):269–281.

Hossain, M., Possart, G., and Steinmann, P. (2010). A finite strain framework for the simulation of polymer curing. part ii. viscoelasticity and shrinkage. *Computational Mechanics*, 46:363–375.

Hossain, M. and Steinmann, P. (2013). More hyperelastic models for rubber-like materials: consistent tangent operators and comparative study. *Journal of the Mechanical Behavior of Materials*, 22:27–50.

Huang, C., Wang, Z., Quinn, D., Suresh, S., and Hsia, K. J. (2018). Differential growth and shape formation in plant organs. *Proceedings of the National Academy of Sciences of the United States of America*, 115(49):12359–12364.

Huang, X., Li, B., Hong, W., Cao, Y.-P., and Feng, X.-Q. (2016). Effects of tension–compression asymmetry on the surface wrinkling of film–substrate systems. *Journal of the Mechanics and Physics of Solids*, 94:88–104.

Ionov, L. (2013). Biomimetic hydrogel-based actuating systems. *Advanced Functional Materials*, 23(36):4555–4570.

Jones, G. and Mahadevan, L. (2015). Optimal control of plates using incompatible strains. *Nonlinearity*, 28(9):3153–3174.

Jones, G. W. and Chapman, S. J. (2012). Modeling growth in biological materials. *SIAM Review*, 54(1):52–118.

Kadapa, C., Li, Z., Hossain, M., and Wang, J. (2021). On the advantages of mixed formulation and higher-order elements for computational morphoelasticity. *Journal of the Mechanics and Physics of Solids*, 148:104289.

Kempaiah, R. and Nie, Z. (2014). From nature to synthetic systems: shape transformation in soft materials. *Journal of Materials Chemistry B*, 2:2357–2368.

Kondaurov, V. and Nikitin, L. (1987). Finite strains of viscoelastic muscle tissue. *Journal of Applied Mathematics and Mechanics*, 51(3):346–353.

Lee, H., Xia, C., and Fang, N. X. (2010). First jump of microgel; actuation speed enhancement by elastic instability. *Soft Matter*, 6(18):4342.

Lee, T., Holland, M. A., Weickenmeier, J., Gosain, A. K., and Tepole, A. B. (2021). The geometry of incompatibility in growing soft tissues: Theory and numerical characterization. *Journal of the Mechanics and Physics of Solids*, 146:104177.

Li, B., Cao, Y.-P., Feng, X.-Q., and Gao, H. (2012). Mechanics of morphological instabilities and surface wrinkling in soft materials: a review. *Soft Matter*, 8:5728–5745.

Liang, H. and Mahadevan, L. (2011). Growth, geometry, and mechanics of a blooming lily. *Proceedings of the National Academy of Sciences*, 108(14):5516–5521.

Liu, Y., Genzer, J., and Dickey, M. D. (2016). "2d or not 2d": Shape-programming polymer sheets. *Progress in Polymer Science*, 52:79–106.

Liu, Y., Li, B., and Feng, X.-Q. (2020). Buckling of growing bacterial chains. *Journal of the Mechanics and Physics of Solids*, 145:104146.

Menzel, A. and Kuhl, E. (2012). Frontiers in growth and remodeling. *Mechanics Research Communications*, 42:1–14.

Mihai, L. A., Budday, S., Holzapfel, G. A., Kuhl, E., and Goriely, A. (2017). A family of hyperelastic models for human brain tissue. *Journal of the Mechanics and Physics of Solids*, 106:60–79.

Mihai, L. A. and Goriely, A. (2020). A plate theory for nematic liquid crystalline solids. *Journal of the Mechanics and Physics of Solids*, 144:104101.

Moulia, B., Douady, S., and Hamant, O. (2021). Fluctuations shape plants through proprioception. *Science*, 372(6540).

Moulton, D. E., Oliveri, H., and Goriely, A. (2020). Multiscale integration of environmental stimuli in plant tropism produces complex behaviors. *Proceedings of the National Academy of Sciences*, 117(51):32226–32237.

Rodriguez, E. K., Hoger, A., and McCulloch, A. D. (1994). Stress-dependent finite growth in soft elastic tissues. *Journal of Biomechanics*, 27(4):455–467.

Sadik, S., Angoshtari, A., Goriely, A., and Yavari, A. (2016). A geometric theory of nonlinear morphoelastic shells. *Journal of Nonlinear Science*, 26:929–978.

Shepherd, R. F., Ilievski, F., Choi, W., Morin, S. A., Stokes, A. A., Mazzeo, A. D., Chen, X., Wang, M., and Whitesides, G. M. (2011). Multigait soft robot. *Proceedings of the National Academy of Sciences of the United States of America*, 108(51):20400–20403.

Siéfert, E., Reyssat, E., Bico, J., and Roman, B. (2019). Bio-inspired pneumatic shape-morphing elastomers. *Nature Materials*, 18:24–28.

Skalak, R., Zargaryan, S., Jain, R., Netti, P., and Hoger, A. (1996). Compatibility and the genesis of residual stress by volumetric growth. *Journal of Mathematical Biology*, 34(8):889–914.

van Doorn, W. G. and Kamdee, C. (2014). Flower opening and closure: an update. *Journal of Experimental Botany*, 65(20):5749–5757.

Wang, J., Song, Z., and Dai, H.-H. (2016). On a consistent finite-strain plate theory for incompressible hyperelastic materials. *International Journal of Solids and Structures*, 78-79:101–109.

Wang, J., Steigmann, D., Wang, F.-F., and Dai, H.-H. (2018). On a consistent finite-strain plate theory of growth. *Journal of the Mechanics and Physics of Solids*, 111:184–214.

Wang, J., Wang, Q., Dai, H.-H., Du, P., and Chen, D. (2019). Shape-programming of hyperelastic plates through differential growth: an analytical approach. *Soft Matter*, 15(11):2391–2399.

Wang, S., Demirci, N., and Holland, M. (2021). Numerical investigation of biomechanically coupled growth in cortical folding. *Biomechanics and Modeling in Mechanobiology*, 20:555–567.

Whitewoods, C. D., Goncalves, B., Cheng, J., Cui, M., Kennaway, R., Lee, K., Bushell, C., Yu, M., Piao, C., and Coen, E. (2020). Evolution

of carnivorous traps from planar leaves through simple shifts in gene expression. *Science*, 367:91–96.

Xu, F., Fu, C., and Yang, Y. (2020). Water affects morphogenesis of growing aquatic plant leaves. *Physical Review Letters*, 124(3):038003.

Yavari, A. (2010). A geometric theory of growth mechanics. *Journal of Nonlinear Science*, 20:781–830.

Yavari, A. (2013). Compatibility equations of nonlinear elasticity for non-simply-connected bodies. *Arch. Rational Mech. Anal.*, 209:237–253.